

Modifications of the Meissner screening profile in $\text{YBa}_2\text{Cu}_3\text{O}_{7-\delta}$ thin films by gold nanoparticles

E. Stilp,^{1,2} A. Suter,¹ T. Prokscha,¹ Z. Salman,¹ E. Morenzoni,¹ H. Keller,² C. Katzer,³ F. Schmidl,³ and M. Döbeli⁴

¹Laboratory for Muon Spin Spectroscopy, Paul Scherrer Institut, CH-5232 Villigen PSI, Switzerland

²Physik-Institut der Universität Zürich, Winterthurerstrasse 190, CH-8057 Zürich, Switzerland

³Institut für Festkörperphysik, Friedrich-Schiller-Universität, Helmholtzweg 5, D-07743 Jena, Germany

⁴Laboratory of Ion Beam Physics, ETH-Zürich, Schafmattstrasse 20, CH-8093 Zürich, Switzerland

(Dated: February 27, 2022)

Adding Au nanoparticles to $\text{YBa}_2\text{Cu}_3\text{O}_{7-\delta}$ thin films leads to an increase of the superconducting transition temperature T_c and the critical current density j_c . While the higher j_c can be understood in terms of a stronger pinning of the flux vortices at the Au nanoparticles, the enhanced T_c is still puzzling. In the present study, we determined the microscopic magnetic penetration profiles and the corresponding London penetration depths λ_L in the Meissner state of optimally doped $\text{YBa}_2\text{Cu}_3\text{O}_{7-\delta}$ thin films with and without Au nanoparticles by low-energy muon spin rotation. By Rutherford backscattering spectrometry, we show that the Au nanoparticles are distributed over the whole thickness of the thin-film samples. The superfluid density $n_s \propto 1/\lambda_L^2$ was found to increase in the films containing Au nanoparticles. We attribute this increase of n_s to a reduction of the defect density possibly due to defect condensation at the Au nanoparticles.

The influence of disorder on cuprate systems is still an open issue. It is known that disorder directly affects the superconducting properties of these systems, but the underlying mechanisms are not fully clarified.¹ In $\text{YBa}_2\text{Cu}_3\text{O}_{7-\delta}$ (YBCO), for instance, the charge carrier transfer from the Cu-O chains to the CuO_2 planes is crucial for the appearance of superconductivity. This charge transfer depends strongly on the oxygen order and on the oxygen mobility within the Cu-O chains.² Substitution of chain Cu by other metal ions leads generally to a suppression of the superconducting transition temperature T_c .³ Surprisingly, this does not apply to Au. Superconducting quantum interference device (SQUID) and neutron diffraction measurements performed by Cieplak *et al.*^{4,5} show that it is possible to incorporate 10 at.% Au into the structure of polycrystalline YBCO, where Au exclusively replaces the chain Cu(1) atoms. This leads to an increase of T_c of about 1.5 K and to an increase of the c -axis lattice constant. The Cu-O bond length between Cu(1) and the oxygen in the Cu-O chains as well as between Cu(1) and the bridging oxygen are enlarged. Previous studies revealed also a lower normal state resistance and a minor influence on the normal state magnetization and on the upper critical field.⁶

Recently, it has been demonstrated that Au nanoparticles, incorporated in YBCO thin films, lead to an increase of T_c and the critical current density j_c (from $4 \cdot 10^7$ A/cm² to $6 \cdot 10^7$ A/cm² at 10 K).^{7,8} Since YBCO is superconducting above the boiling temperature of nitrogen this is of special interest for applications. A stronger flux pinning of the vortices at the Au nanoparticles causes a higher j_c , which is crucial in order to improve superconducting magnetic field sensors^{8,9} as used in dc-SQUID gradiometers.

Until now little is known about the effect of the inclusion of Au nanoparticles on the microscopic superconducting parameters, such as the superfluid density n_s . In the present study we investigated two sets of YBCO thin

films with different Au contents by means of low-energy muon spin rotation (LE- μ SR) experiments and Rutherford backscattering spectrometry (RBS). The amount and the distribution of the Au nanoparticles were determined as well as the microscopic changes of the Meissner screening profile and the London penetration depth λ_L . This is of special interest, since λ_L is related to the superfluid density n_s :

$$\lambda_L^2 \propto \frac{m^*}{n_s}, \quad (1)$$

where m^* is the effective mass of the supercarriers.

The optimally doped YBCO thin films studied in this work were prepared by pulsed-laser-deposition (PLD) using a KrF excimer laser ($\lambda = 248$ nm, $\tau = 25$ ns) at the Friedrich-Schiller-Universität in Jena. Single-crystal SrTiO_3 $10 \times 10 \times 1$ mm³ in size and polished with the surface perpendicular to the [001] crystal axis was used as substrate. In order to realize clustered Au nanoparticles, an initial gold seed layer of 1.8 nm thickness was sputtered on the substrates by dc-magnetron sputtering ($I = 10$ mA, $U = 215$ V, growth rate: 4 nm/min, $p_{\text{Ar}} = 5$ mbar). Subsequently, the Au coated substrates were heated to 780°C to achieve a dewetting of the Au seed layer. The resulting nanoparticles were overgrown by YBCO in an in situ process. The YBCO deposition was realized by a PLD process in an oxygen atmosphere (repetition rate: 5 Hz, laser fluence: 2.2 J/cm², growth rate: 20 nm/min, $p_{\text{O}_2} = 0.5$ mbar). In order to obtain the orthorhombic phase, the resulting YBCO thin films were cooled down to room temperature at a rate of 50 K/min in pure oxygen ($p_{\text{O}_2} = 800$ mbar). The resulting optimally doped YBCO thin films have a typical thickness of 120 – 200 nm and are c -axis oriented. With the Au seed layer thickness used the typical Au particle size is in the range 10 – 40 nm.⁸ The area distribution of the Au nanoparticles is quite homogeneous, whereas the concentration within the depth profile varies, as later discussed.

More details on the growth and the properties of the used samples can be found in Refs. 7 and 8. The mean distance between the Au nanoparticles is about 50 nm. The samples are therefore still in the clean limit, since the correlation length is of the order of 2 nm.

Here, we studied two sample sets with (YBCO_{Au}) and without (YBCO) Au nanoparticles. As expected, slightly higher T_c values were observed by resistivity measurements for the YBCO_{Au} compared to the pristine YBCO thin-film samples (see Fig. 1). In order to monitor precisely the amount as well as the distribution of Au as a function of depth in the thin-film samples, RBS measurements were performed at ETH Zürich. For RBS a ^4He beam with an energy of 2–5 MeV and a silicon PIN diode detector at a scattering angle of 168° were used.¹⁰ The elemental composition was determined by using the RUMP software.¹¹ In the YBCO samples no Au peak is present in the RBS spectra as expected. The stoichiometry of optimally doped YBCO was confirmed within experimental uncertainty. The Au concentrations as function of depth were determined in the YBCO_{Au} samples as depicted in Fig. 2. In these samples the Au nanoparticles are distributed over the whole superconducting region. On average there are about $4(1) \cdot 10^{15}$ Au atoms/cm² in this region. The so-called dead layer close to the substrate interface d_{DL} contains less nanoparticles and exhibits no macroscopic Meissner screening. This is consistent with the lower T_c generally observed in this region in these thin-film samples.¹²

In order to determine the Meissner screening profile $B(z)$ and the temperature dependence of the magnetic penetration depth λ_L in a straight forward way LE- μSR experiments were performed at the μE4 beamline at the Paul Scherrer Institut (PSI, Switzerland).^{13,14} A mo-

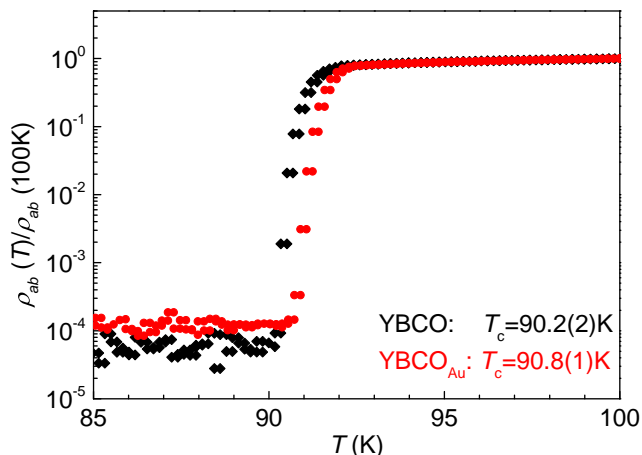


FIG. 1. (Color online) In-plane resistivity ρ_{ab} normalized at 100 K versus temperature T of PLD-grown optimally doped YBCO thin-film samples: YBCO (black diamonds) and YBCO_{Au} (red circles). The listed values of the superconducting transition temperatures T_c are defined by $\rho_{ab}(T_c)/\rho_{ab}(100\text{K}) \leq 2.5 \cdot 10^{-4}$. They are averaged over five measurement cycles (heating and cooling).

saic of four samples from one set was glued with silver paint on a nickel coated aluminum plate. The low-energy muons (μ^+) are produced at a rate of about 10^4s^{-1} using a solid Ar/N₂ moderator. After reacceleration the final energy of the muons is adjusted by a bias voltage at the sample. By tuning the energy between 5 and 25 keV the mean stopping depth of the muons can be varied in a range of 25 – 106 nm in YBCO (see Fig. 3).

In condensed matter, muons act as local magnetic probes. Measuring the time difference $t = t_e - t_s$ between the implantation time t_s and the decay time t_e of the μ^+ , detected via the decay positron, allows one to determine the temporal evolution of the muon-spin polarization $P(t)$.¹⁶ This is possible due to the parity violation of the weak decay which results in a positron emission preferentially along the μ^+ spin direction at the time of decay. The positron count rate $N(t)$ is given by:

$$N(t) = N_0 e^{-t/\tau_\mu} [1 + AP(t)] + N_{\text{Bkg}}, \quad (2)$$

with a mean μ^+ lifetime of $\tau_\mu = 2.197\text{ }\mu\text{s}$, where N_0 gives the scale of the counted positrons, N_{Bkg} is a time-independent background of uncorrelated events, and A is the observable decay asymmetry.

The experiments were performed in the Meissner state. After zero field cooling to 5 K a magnetic field $B_{\text{ext}} = 8\text{ mT} < \mu_0 H_{c1}$ is applied parallel to the thin-film surfaces and perpendicular to the initial muon spin. In this case the muon-spin polarization $P(t)$ is given by

$$P(t) = e^{-\sigma^2 t^2/2} \int n(z) \cos[\gamma_\mu B(z)t + \phi] dz, \quad (3)$$

with the initial phase ϕ , the muon gyromagnetic ratio $\gamma_\mu = 2\pi \cdot 135.5\text{ MHz/T}$, and the depolarization rate σ

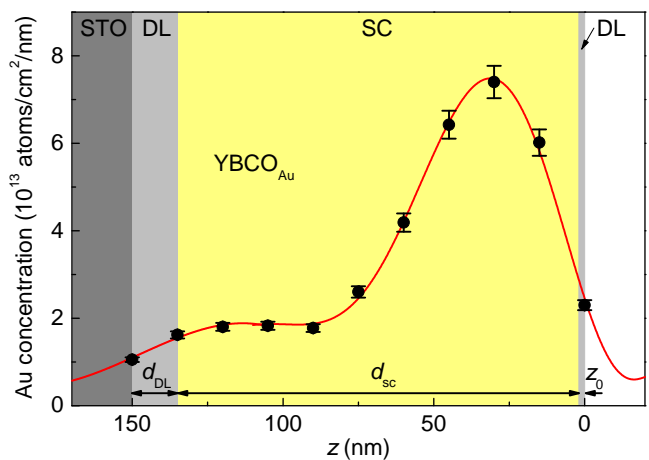


FIG. 2. (Color online) Gold concentration versus depth z along the crystallographic c -axis for a YBCO_{Au} thin-film sample determined by RBS. The different regions are labeled: STO is the substrate region (dark gray), DL is the dead layer at the substrate (d_{DL}) and at the vacuum (z_0) interface (light gray), SC is the superconducting region with thickness d_{sc} (yellow). The red line is a guide to the eye.

TABLE I. Summary of the parameters determined for the investigated optimally doped YBCO thin-film samples with (YBCO_{Au}) and without Au nanoparticles (YBCO). The superconducting transition temperatures T_c were obtained from resistivity measurements. The average film thicknesses \bar{d} were extracted from RBS measurements. From a global fit of the LE- μ SR data the superconducting thicknesses d_{sc} , the dead layer thicknesses to the vacuum interface z_0 , and the London penetrations depths $\lambda_{ab}(10\text{K})$ were determined. $\lambda_{ab}(0\text{K})$ and the superconducting gap Δ_0 were extracted from a linear fit in the range 5 – 35 K of $\lambda_{ab}(T)$ measured with LE- μ SR. For comparison single crystal values²⁰ are also presented.

Sample	T_c (K)	\bar{d} (nm)	d_{sc} (nm)	z_0 (nm)	$\lambda_{ab}(10\text{K})$ (nm)	$\lambda_{ab}(0\text{K})$ (nm)	Δ_0 (meV)
YBCO film	90.2(2)	150(8)	119(1)	0(2)	161(1)	158(1)	22(2)
YBCO _{Au} film	90.8(1)	152(8)	133(1)	1(2)	154(1)	150(1)	24(2)
YBCO bulk ²⁰	94.1(1)			10.3(5)		115(4)	20(4)

which is a measure of any inhomogeneous local magnetic field distribution at the μ^+ site. The muon stopping distributions $n(z)$ for different energies are simulated using the Monte Carlo code TRIM.SP¹⁵ (see Fig. 3). The applicability of the TRIM.SP code for low energy muons stopping in matter is demonstrated in Ref. 17. Since the thin films have twinned a - and b -axes, the average magnetic penetration depth λ_{ab} is determined with the present experimental set-up. To analyze the data, the London model profile for thin films was used, resulting from an exponential decay of B_{ext} from both interfaces:

$$B(z) = \begin{cases} B_{ext} \frac{\cosh\left(\frac{z - z_0 - d_{sc}/2}{\lambda_{ab}}\right)}{\cosh\left(\frac{d_{sc}/2}{\lambda_{ab}}\right)} & , z \geq z_0 \\ B_{ext} & , z < z_0 \end{cases} \quad (4)$$

where d_{sc} is the thickness of the superconducting region, z is the depth along the c -axis, and z_0 is the effective dead layer at the vacuum interface (see Fig. 2). This dead layer may be due to the roughness of the surface¹⁸ or to a reduction of the order parameter close to the surface.

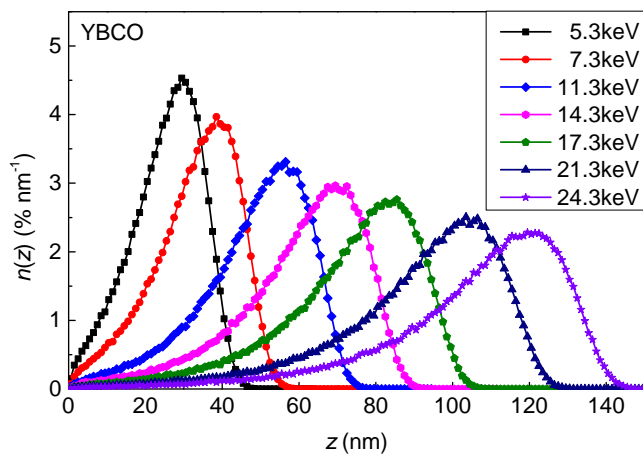


FIG. 3. (Color online) The normalized stopping distribution of positively charged muons $n(z)$ for different implantation energies (see inset) of a 150 nm thick YBCO film simulated with TRIM.SP.¹⁵ The lines are guides to the eye.

By the simultaneous analysis of the μ SR spectra measured at seven different implantation energies at 10 K, the Meissner screening profiles of the two sample sets YBCO and YBCO_{Au} were determined (see Fig. 4). The resulting values of the parameters are listed in Table I. The thickness of the superconducting layer d_{sc} is substantially smaller than the average film thickness \bar{d} in both sample sets. This confirms the presence of a dead layer at the substrate interface d_{DL} of about 31 nm for YBCO and about 18 nm for YBCO_{Au}. The interface layer (d_{DL}) exhibits only weak superconductivity as mentioned before. No macroscopic Meissner screening is observed in this region. This could be explained by the presence of grain boundaries due to mechanical strain,¹² leading also to the reduction of T_c in thin films compared to single-crystal YBCO. Note that d_{DL} is smaller for the YBCO_{Au} samples, indicating that the Au nanoparticles may relax the mechanical strain. The dead layers to the vacuum

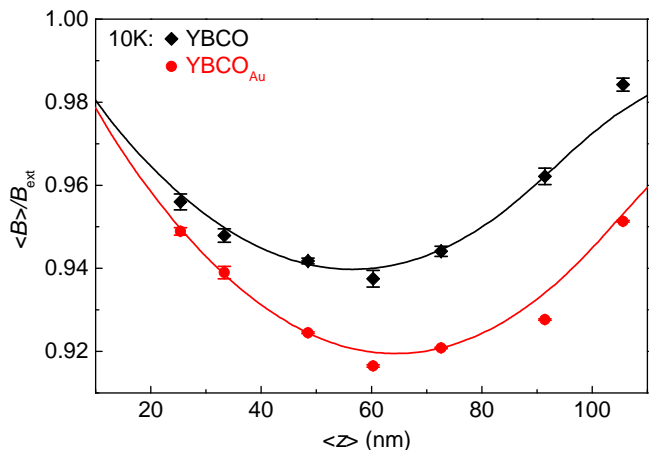


FIG. 4. (Color online) The average local magnetic field normalized to the applied field $\langle B \rangle / B_{ext}$ versus the mean muon implantation depth $\langle z \rangle$ measured in an applied magnetic field $B_{ext} = 8\text{ mT}$ parallel to the film surface at 10 K for thin-film YBCO and YBCO_{Au}. The solid lines represent the results of the global fits obtained with musrfit,¹⁹ where seven μ SR spectra with different energies were analyzed simultaneously. The used parameter values are listed in Table I. The data points are determined from single energy fits using $\langle B \rangle = \int n(z)B(z)dz$, where $n(z)$ is the muon implantation profile of the corresponding energy (see Fig. 3).

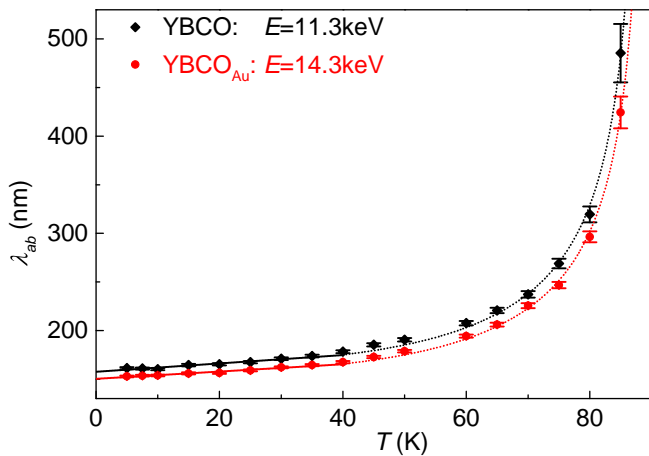


FIG. 5. (Color online) The London penetration depth λ_{ab} versus temperature T for thin-film YBCO and YBCO_{Au}. λ_{ab} was determined from $\langle B \rangle / B_{\text{ext}}$ (Gaussian fit to the μSR spectra with `musrfit`¹⁹) by using the parameters from the global fit determined at 10 K. The applied magnetic field was $B_{\text{ext}} = 8 \text{ mT}$. The implantation energies E given in the figure were selected according to the minimum in $\langle B \rangle / B_{\text{ext}}$. The corresponding solid lines are linear fits to the data in the range 5 – 35 K by means of Eq. (5). The parameter values are listed in Table I. The dotted lines are fits to the power law $\lambda_{ab}(T) = \lambda_{ab}(0)[1 - (T/T_c)^n]^{-1/2}$ with $n \simeq 2.7$.

interface are surprisingly small in both sets ($z_0 \approx 1 \text{ nm}$) compared to single-crystal YBCO ($z_0 \simeq 10 \text{ nm}$)²⁰ and other YBCO thin-film measurements ($z_0 \simeq 8 \text{ nm}$).²¹

YBCO_{Au} screens the magnetic field better, and therefore exhibits a smaller λ_{ab} than our pristine YBCO (Fig. 4). The temperature dependence of λ_{ab} of thin-film YBCO and YBCO_{Au} is presented in Fig. 5. These values of λ_{ab} were extracted from μSR spectra measured at the energy corresponding to the minimal average local magnetic field $\langle B \rangle_{\text{min}}$ at 10 K. Both sample sets show a linear increase in λ_{ab} up to 35 K which is characteristic for a d -wave pairing:²²

$$\lambda_{ab}(T) = \lambda_{ab}(0\text{K}) \cdot [1 + \ln(2) \cdot k_B T / \Delta_0]. \quad (5)$$

The slopes for YBCO and YBCO_{Au} are very similar ($\approx 0.4 \text{ nm/K}$), so the superconducting gaps Δ_0 are the same within experimental uncertainty (see Table I). The value of $\lambda_{ab}(0\text{K})$ for YBCO_{Au} is smaller compared to YBCO, but still larger than that one of single-crystal YBCO. If the amount of Au nanoparticles is higher (Au seed layer of 3 nm instead of 1.8 nm) the same effects on T_c and λ_{ab} were observed. The nominal changes are

smaller, since most of the Au nanoparticles remained at the interface to the substrate.

A possible explanation for the reduced magnetic penetration depth in YBCO_{Au} is the diffusion of Au from the nanoparticles into the Cu-O chains (likely during the YBCO deposition), since Au has a relatively high mobility at higher temperatures. A replacement of Cu(1) by Au in the Cu-O chains leads to an increase of the oxygen mobility.²³ An enhanced oxygen mobility favors longer Cu-O chain segments leading to an increase of the charge carrier transfer from the Cu-O chains to the CuO₂ planes.² Since more charge carriers can contribute to superconductivity, n_s increases while λ_{ab} decreases. In this case the c -axis lattice constant should be slightly increased.⁴ This, however, was not observed in the investigated samples.

Another possibility is that the presence of Au nanoparticles in the superconducting region of YBCO lowers the defect density and leads therefore to the observed reduction of λ_{ab} in YBCO_{Au}. A reduced defect density could originate from a condensation of defects at the Au nanoparticles, so that the CuO₂ planes and the structure are less disturbed. To evaluate the defect density we take the c -axis lattice constant as an indication. In YBCO_{Au}, we observe a slightly smaller c -axis lattice constant ($c_{\text{YBCO}_{\text{Au}}} = 1.1688(2) \text{ nm} < c_{\text{YBCO}} = 1.1699(2) \text{ nm}$). YBCO single crystals have an even smaller c -axis lattice constant ($c_{\text{bulk}} = 1.167(1) \text{ nm}$).²⁴ A lower defect density is generally expected in single-crystal YBCO compared to thin-film YBCO which is consistent with the trend of the c -axis lattice constants. From this point of view YBCO_{Au} has a lower defect density than our pristine YBCO, but a higher one compared to single-crystal YBCO. Since single-crystal YBCO has also a smaller λ_{ab} and a higher T_c compared to our YBCO and YBCO_{Au} samples, a reduced defect density is a possible reason for the slightly different values of T_c and $\lambda_{ab}(0)$ in YBCO_{Au} compared to pure YBCO films.

In summary, we have shown by using LE- μSR that the increase of T_c in thin-film YBCO containing Au nanoparticles is accompanied by a reduction of the average magnetic penetration depth λ_{ab} . We attribute this reduction to a lowered defect density. The diffusion of Au into the Cu-O chains may also contribute to the observed changes of T_c and n_s . In previous studies on YBCO, Cu was exchanged by Au within the Cu-O chains to obtain an enhanced T_c . Our results indicate that the presence of Au nanoparticles has a similar effect in thin-film YBCO.

We acknowledge Hans-Peter Weber for his excellent technical support. This work was partly supported by the Swiss National Science Foundation and the Landesgraduiertenförderung Thüringen.

¹ H. Alloul, J. Bobroff, M. Gabay, and P. J. Hirschfeld, *Rev. Mod. Phys.* **81**, 45 (2009).

² A. A. Aligia and J. Garcés, *Phys. Rev. B* **49**, 524 (1994).

³ L. Shlyk, G. Krabbes, G. Fuchs, G. Stöver, S. Gruss, and K. Nenkov, *Physica C* **377**, 437 (2002).

⁴ M. Z. Cieplak, G. Xiao, C. L. Chien, J. K. Stalick, and J.

- J. Rhyne, *Appl. Phys. Lett.* **57**, 934 (1990).
- ⁵ M. Z. Cieplak, G. Xiao, C. L. Chien, A. Bakshai, D. Artymowicz, W. Bryden, J. K. Stalick, and J. J. Rhyne, *Phys. Rev. B* **42**, 6200 (1990).
- ⁶ U. Welp, S. Fleshler, W. K. Kwok, J. Downey, G. W. Crabtree, H. Claus, A. Erb, and G. Müller-Vogt, *Phys. Rev. B* **47**, 12369 (1993).
- ⁷ C. Katzer, M. Westerhausen, I. Uschmann, F. Schmidl, U. Hübner, and P. Seidel, *Supercond. Sci. Technol.* **26**, 125008 (2013).
- ⁸ C. Katzer, M. Schmidt, P. Michalowski, D. Kuhwald, F. Schmidl, V. Grosse, S. Treiber, C. Stahl, J. Albrecht, U. Hübner, A. Undisz, M. Rettenmayr, G. Schütz, and P. Seidel, *EPL* **95**, 68005 (2011).
- ⁹ C. Katzer, C. Stahl, P. Michalowski, S. Treiber, F. Schmidl, P. Seidel, J. Albrecht, and G. Schütz, *New J. Phys.* **15**, 113029 (2013).
- ¹⁰ M. Döbeli, *J. Phys.: Condens. Matter* **20**, 264010 (2008).
- ¹¹ L. R. Doolittle, *Nucl. Instrum. Methods Phys. Res. B* **15**, 227 (1986).
- ¹² H. Schneidewind, F. Schmidl, S. Linzen, and P. Seidel, *Physica C* **250**, 191 (1995).
- ¹³ E. Morenzoni, T. Prokscha, A. Suter, H. Luetkens, and R. Khasanov, *J. Phys.: Cond. Matt.* **16**, S4583 (2004).
- ¹⁴ T. Prokscha, E. Morenzoni, K. Deiters, F. Foroughi, D. George, R. Kobler, A. Suter, and V. Vrankovic, *Nucl. Instrum. Methods Phys. Res., Sect. A* **595**, 317 (2008).
- ¹⁵ W. Eckstein, *Computer Simulation of Ion-Solid Interactions* (Springer, Berlin, 1991).
- ¹⁶ A. Yaouanc and P. Dalmass de Reotier, *Muon Spin Rotation, Relaxation, and Resonance: Applications to Condensed Matter* (Oxford University Press, Oxford, 2011); V. P. Smilga and Yu. M. Belousov, *The Muon Method in Science* (Nova Science Publishers, New York, 1994).
- ¹⁷ E. Morenzoni, H. Glückler, T. Prokscha, R. Khasanov, H. Luetkens, M. Birke, E. M. Forgan, Ch. Niedermayer, and M. Pleines, *Nucl. Instr. Meth. B* **192**, 254 (2002).
- ¹⁸ M. Lindstrom, B. Wetton, and R. Kiefl, *J. Eng. Math.*, DOI 10.1007/s10665-013-9640-y.
- ¹⁹ A. Suter and B. M. Wojek, *Physics Procedia* **30**, 69 (2012).
- ²⁰ R. F. Kiefl, M. D. Hossain, B. M. Wojek, S. R. Dunsiger, G. D. Morris, T. Prokscha, Z. Salman, J. Baglo, D. A. Bonn, R. Liang, W. N. Hardy, A. Suter, and E. Morenzoni, *Phys. Rev. B* **81**, 180502(R) (2010).
- ²¹ T. J. Jackson, T. M. Riseman, E. M. Forgan, H. Glückler, T. Prokscha, E. Morenzoni, M. Pleines, Ch. Niedermayer, G. Schatz, H. Luetkens, and J. Litterst, *Phys. Rev. Lett.* **84**, 4958 (2000).
- ²² C. P. Poole Jr., H. A. Farach, R. J. Creswick, and R. Prozorov, *Superconductivity* (Academic Press, London, 2007).
- ²³ H. Claus, S. Yang, H. K. Viswanathan, G. W. Crabtree, J. W. Downey, and B. W. Veal, *Physica C* **213**, 185 (1993).
- ²⁴ P. Benzi, E. Bottizzo, and N. Rizzi, *J. Cryst. Growth* **269**, 625 (2004).